Shape formation of helical ribbons induced by material anisotropy

Xiaojiao Yu, Lina Zhang, Nan Hu, Hannah Grover, Shicheng Huang, Dong Wang, and Zi Chen

Citation: Appl. Phys. Lett. **110**, 091901 (2017); doi: 10.1063/1.4977090
View online: http://dx.doi.org/10.1063/1.4977090
View Table of Contents: http://aip.scitation.org/toc/apl/110/9
Published by the American Institute of Physics

Shape formation of helical ribbons induced by material anisotropy

Xiaojiao Yu,[1,a)] Lina Zhang,[1,2,a)] Nan Hu,[1] Hannah Grover,[1] Shicheng Huang,[1] Dong Wang,[1] and Zi Chen[1,b)]
[1]*Thayer School of Engineering, Dartmouth College, Hanover, New Hampshire 03755, USA*
[2]*Department of Engineering Mechanics, Shanghai Jiao Tong University, Shanghai 200240, China*

(Received 2 November 2016; accepted 12 January 2017; published online 27 February 2017)

Helices are ubiquitous building blocks in natural and engineered systems. Previous studies showed that helical ribbon morphology can result from anisotropic driving forces and geometric misorientation between the principal axes of the driving forces and the geometric axes. However, helical ribbon shapes induced by elastic modulus anisotropy have not been systematically examined even though most natural and engineered structures are made of composite materials with anisotropic mechanical properties. We build on a previously developed model using continuum elasticity and stationarity principles to predict helical ribbon shapes induced by material anisotropy under both isotropic and anisotropic pre-stretching conditions. Results from finite element analysis and table-top experiments showed that the principal curvatures, chirality, and helix angles can be further tuned in anisotropic ribbons under both isotropic and anisotropic pre-stretching conditions. This work can promote programmable design and fabrication of curved structures and devices. *Published by AIP Publishing.*
[http://dx.doi.org/10.1063/1.4977090]

Helices are ubiquitous in natural and engineered systems at all length scales, including DNA,[1] seed pods,[2,3] spores,[4] mechanical springs,[5] and nematic elastomers.[6] Stable morphologies of ribbons include rings, pure twisted ribbons, and spiral helical ribbons. They form as a result of the competition between bending energy and stretching energy. The driving force can come from surface or interfacial stress,[7–9] edge stress,[10] misfit strain,[11,12] residual stress,[13] differential growth,[14] and swelling.[2] This energy competition can also result in shape transition from a purely twisted to a cylindrical helical ribbon depending on the interactions between stress, preferred molecular orientations, and chirality.[15–19] Their remarkable tunability makes helical ribbons promising structural prototypes for a wide range of applications in nanoelectromechanical systems (NEMS),[20] drug delivery,[21] micro-robotics,[22,23] optoelectronics,[24] and bioinspired devices.[13,25]

Recent research has extensively documented the form that helical ribbons assume when induced by mechanical anisotropy.[8,26–30] Chen *et al.* employed the continuum elasticity theory to predict the morphology of the helical ribbons driven by isotropic or anisotropic surface stresses.[7,31] Armon *et al.* developed a theoretical model to interpret the formation of helical seedpods.[2] Most of the previous studies on helical ribbon formation assumed isotropic material properties;[2,7,31] however, the material properties in many physical systems are anisotropic.[4,32–34] For example, honey locust seed pods can develop helical shapes as shown in Fig. 1. This morphogenesis process has inspired us to look into how principal curvatures, chirality, and helix angles are affected by anisotropic material properties. A comprehensive understanding on the effects of the material anisotropy can inspire new ways of controlling the shape formation and transition in spontaneously bent and twisted structures.[35–37]

We began by conducting a series of table-top experiments using the strain engineering method,[5] where bi-axial pre-strains were imposed in to induce the formation of helical shapes. In this study, a piece of latex rubber sheet was pre-stretched 40% in both x and y directions. An unstrained elastic strip is bonded to the strained latex sheet on one side and to another unstrained latex sheet on the other side, in which case the driving forces are isotropic and the resulting deformation is equivalent to that of a ribbon subjected to

FIG. 1. Helical seed pods of Honey Locust trees.

[a)]X. Yu and L. Zhang contributed equally to this work.
[b)]Author to whom correspondence should be addressed. Electronic mail: zi.chen@dartmouth.edu

isotropic surface stress.[5] To create anisotropic driving forces, an unstrained adhesive tape is bonded to two latex rubber sheets on each side. The bottom sheet is pre-stretched 40% in the horizontal direction and top sheet is pre-stretched 40% in the vertical direction.[38] To introduce the material anisotropy, we arranged an array of Nitinol wires between the upper side of the adhesive tape and the top latex sheet. Wires are all placed along the y axis with an equal spacing of 2.5 mm in between to produce the anisotropic elastic modulus. The strips were oriented at a misorientation angle θ with the x-axis between 0 and $\pi/2$ with an interval of $\pi/12$. The geometry of the ribbons satisfies the following conditions: length $l \gg$ width w and $w \gg$ thickness h (Fig. 2). x' and y' denote the longitudinal and transverse axes, respectively.

The transformation equations for strain in x', y' are given as

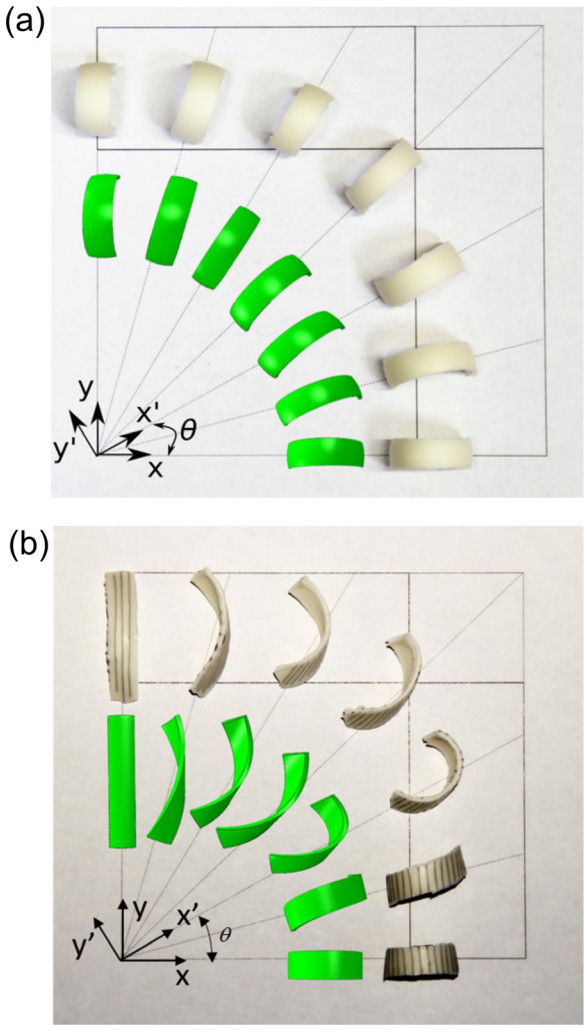

FIG. 2. Stable configurations of tri-layer ribbons (both experimental and simulation results) with the bottom layer under isotropic mechanical pre-stretch (40% biaxial pre-stretching in both x and y directions). (a) Isotropic ribbons where the top layer (with a thickness of 0.15 mm) is the same latex sheet as the bottom layer but without stretching. Young's modulus and Poisson's ratio are 1.8 MPa and 0.49, respectively. The elastic strip comprising the middle layer ($h = 1.43$ mm) has a Young's modulus and Poisson's ratio of 2.0 MPa and 0.37, respectively. (b) Anisotropic ribbons where NiTi wires have been placed between the top layer and the middle layer. The spacing between the wires is 2.5 mm, the diameter is 0.2 mm, the Young's modulus is 60.9 GPa, and the Poisson's ratio is 0.33.

$$\begin{aligned}
\varepsilon_{x'x'} &= \varepsilon_{xx}\cos^2\theta + \varepsilon_{yy}\sin^2\theta + \gamma_{xy}\sin\theta\cos\theta \\
\varepsilon_{y'y'} &= \varepsilon_{xx}\sin^2\theta + \varepsilon_{yy}\cos^2\theta - \gamma_{xy}\sin\theta\cos\theta \\
\gamma_{x'y'} &= 2(\varepsilon_{yy} - \varepsilon_{xx})\sin\theta\cos\theta + \gamma_{xy}(\cos^2\theta - \sin^2\theta).
\end{aligned} \tag{1}$$

Finite element (FE) simulations were conducted using the commercial software ABAQUS to obtain the formation of helical shapes after pre-stretch is released. The tri-layer system is assumed to exhibit large deformation similar to the response of hyper-elastic materials with 40% of pre-stretch. Tri-layer without NiTi wire embedded is assumed to be isotropic. The spacing between the wires is 2.5 mm and the diameter is 0.2 mm. Models were built using quadratic solid elements (element type C3D20R) with a total of 14 713 nodes and 3000 elements for the mesh geometry.[39] The Neo-Hookean model was adopted as the material model. An equal-biaxial pre-strain applied at the bottom layer of the model to simulate the mechanical isotropic case. A pre-strain applied at the x direction of the bottom layer and y direction of the top layer was used for the mechanical anisotropic case. The ABAQUS static solver is employed for all the simulations with the consideration of the NLgeom algorithm. The pre-strain effect is implemented in ABAQUS through UMAT, the subroutine to define a material's mechanical properties. The degrees of freedom of one corner point is set to be zero as the boundary condition.

In the first group, we started with the scenario of mechanical and material isotropy when the bottom rubber sheet is equal-biaxially pre-stretched by 40% ($\varepsilon_{xx} = \varepsilon_{yy} = 40\%$, $\gamma_{xy} = 0\%$) and no wires were embedded (see Fig. 2(a)). It can be shown that no matter what θ is, $\varepsilon_{x'x'} = \varepsilon_{y'y'} = \varepsilon_{xx}, \gamma_{x'y'} = 0$. Therefore, it was inferred that deformed ribbon shapes should be the same regardless of the θ value. According to our previous work,[7] the ribbon forms a ring when either two principal curvatures $\kappa_x = \kappa_y$, $\theta = 0$, or $\theta = \pi/2$. We further performed FE simulations (as detailed above) to validate the above predictions. It can be seen in Fig. 2(a) that simulated, deformed shapes are consistent with the experiments.

In the second group, the rubber sheets were stretched the same way as in the first group but we introduced material anisotropy by attaching Nitinol wires between the top-layer rubber sheet and the bottom-layer strip along the y-axis such that ribbons' mechanical properties become anisotropic (more specifically, orthotropic in this case), see Fig. 2(b). The wires were equally spaced, all aligned in the y-direction, and arranged in such a way that the volume fraction of wires is the same for different θ values. As expected, $\varepsilon_{x'x'} \neq \varepsilon_{y'y'}$ and $\gamma_{x'y'} \neq 0$ unless $\sin\theta\cos\theta = 0$, i.e., θ is 0 or $\pi/2$ (proof in the supplementary material). The deformed shape of the ribbons varies as a function of θ. When θ is 0 or $\pi/2$, a ring shape still forms, but the two principal curvatures are no longer the same because of the elastic anisotropy. More specifically, because elastic modulus $E_y > E_x$, two principal curvatures along the x- and y-directions $\kappa_x > \kappa_y$ (see supplementary material). Finite element simulations confirmed the formation of ring-like shapes with $\theta = 0$ and $\pi/2$ when the mechanical properties became anisotropic. Right-handed helical ribbons formed and the shapes are dependent upon the misorientation angle ($\theta \in (0, \pi/2)$) between the principal axes of the stiffness tensor and the geometric axes (Fig. 2(b)). Here, a biaxial pre-strain of

40% was chosen to showcase the formation of helical ribbons when the material anisotropy was introduced. Different values of pre-strains will necessarily give rise to different helical ribbon shapes as the shape is controlled by the pre-strains, the elastic properties, and the density and orientation of the embedded wires, but the mechanical principle stays the same.

In the third group, we considered the effects of anisotropic driving forces in isotropic ribbons by uniaxially pre-stretching the bottom sheet in the x-direction by 40% and the top sheet in the y-direction by 40%. The deformation should be equivalent to the scenario when only the bottom sheet is pre-stretched in the x-direction by 40% and pre-compressed in the y-direction by 40%, i.e., $\varepsilon_{xx} = -\varepsilon_{yy} = 40\%$. Equation (1) reduces to

$$\begin{aligned} \varepsilon_{x'x'} &= \varepsilon_{xx}(\cos^2\theta - \sin^2\theta) \\ \varepsilon_{y'y'} &= \varepsilon_{xx}(\sin^2\theta - \cos^2\theta) \\ \gamma_{x'y'} &= -4\varepsilon_{xx}\sin\theta\cos\theta. \end{aligned} \tag{2}$$

For the isotropic materials as shown in Fig. 3(a), when θ is 0, $\varepsilon_{x'x'} = \varepsilon_{xx}$, $\varepsilon_{y'y'} = -\varepsilon_{xx}$, and $\gamma_{x'y'} = 0$. As expected, the deformed ribbon was a ring with two principal curvatures, κ_x and κ_y, such that $\kappa_x = -\kappa_y$. Similarly, when θ *is* $\pi/2$, another ring with principle curvatures of opposite signs formed since $\varepsilon_{x'x'} = -\varepsilon_{xx}$, $\varepsilon_{y'y'} = \varepsilon_{xx}$, and $\gamma_{x'y'} = 0$. In contrast, when θ *is* $\pi/4$, $\varepsilon_{x'x'} = \varepsilon_{y'y'} = 0$ and $\gamma_{x'y'} = -2\varepsilon_{xx}$, suggesting that the ribbon should form a purely twisted shape, which is verified by our experiment. As the angle θ increased from 0 to $\pi/4$, the shape transitioned from a ring to a right-handed helical ribbon and to a purely twisted helical shape when the angle reached $\pi/4$. As the angle further increased, right-handed helical ribbons formed again. Another ring shape formed when $\theta = \pi/2$.

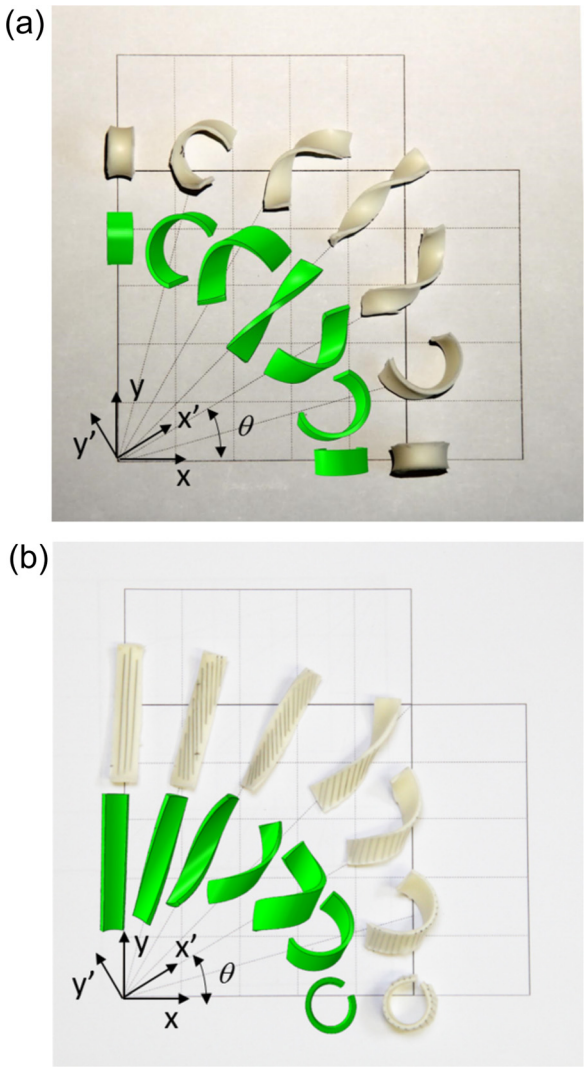

FIG. 3. Experimental and simulation results of the helical ribbons showing mechanical anisotropic pre-stretch. The bottom layer was pre-stretched in the x direction for 40% and the top layer was pre-stretched in the y direction for 40%. (a) Isotropic ribbons with the material property the same as in Fig. 2. (b) Anisotropic ribbons where NiTi were equally spaced between the middle layer and top layer.

In the last group, we introduced the material anisotropy by adding an array of Nitinol wires to the ribbons while maintaining the same pre-stretches as in the third group. The altered elastic properties resulted in significant changes of the helical ribbon shapes (see Fig. 3(b)). At $\theta = 0$ and $\pi/2$, a ring still formed; however, the two principal curvatures no longer had the same magnitude, i.e., $\kappa_x \neq -\kappa_y$. In between, right-handed helical ribbons were obtained again. At $\theta = \pi/4$, however, it did not form a purely twisted shape as in the previous case. Since the elastic moduli changed with the addition of wires, the principal curvatures became different from those in isotropic ribbons, and so were the helix angle and radius.

Helix angles (φ) and radius of all the tested conditions were calculated with the following equation:[19]

$$\begin{aligned} \Phi &= \arcsin\left(\frac{\tau}{\alpha}\right) = \arcsin\left\{\frac{(\kappa_1 - \kappa_2)\sin\theta\cos\theta}{\sqrt{{\kappa_1}^2\cos^2\theta + {\kappa_2}^2\sin^2\theta}}\right\}, \\ R &= \left|\frac{\kappa_1\cos^2\theta + \kappa_2\sin^2\theta}{{\kappa_1}^2\cos^2\theta + {\kappa_2}^2\sin^2\theta}\right|, \end{aligned} \tag{3}$$

where $\tau = (\kappa_1 - \kappa_2)\sin\theta\cos\theta$ and $\alpha = \sqrt{{\kappa_1}^2\cos^2\theta + {\kappa_2}^2\sin^2\theta}$ by first obtaining κ_1 and κ_2 for the four sets of experiments. The two principal curvatures κ_1 and κ_2 are essentially the curvatures κ_x and κ_y along the x and y directions, which can be obtained by taking the inverse of the measured radii of the rings formed at 0 and $\pi/2$ for each group. In Fig. 4, the helix angle and radius are plotted against θ values to characterize the helix. The helix angles in group 1 are all zero, which is consistent with experimental and simulation results shown in Fig. 2(a), where ribbons all form rings with the same radius for different θ values. Under similar loading conditions but with nitinol wires embedded, the helix angle first increases until θ reaches $\pi/3$ and then decreases again to 0 when θ reaches $\pi/2$ (Fig. 4(a)). In contrast, the radius increases monotonically as θ increases from 0 to $\pi/2$ (Fig. 4(b)). For group 3, the helix angle increases linearly from 0 to $\pi/2$, when θ increases from 0 to $\pi/4$; in fact, the helix angle is equal to 2θ according to Eq. (3). Then, the helix angle decreases linearly to 0 as θ increases from $\pi/4$ to $\pi/2$ since the helix angle in this case is equal to π-2θ. As θ increases, the radius decreases to 0 when the ribbon becomes a purely twisted shape at $\theta = \pi/4$ and then gets larger as θ increases.

Lastly, in group 4 (under the same loading condition as in group 3 but with embedded wires) the helix angle increases first with θ and reaches a maximum value when $\theta = \pi/3$. Then, it decreases to 0 at $\theta = \pi/2$. The radius

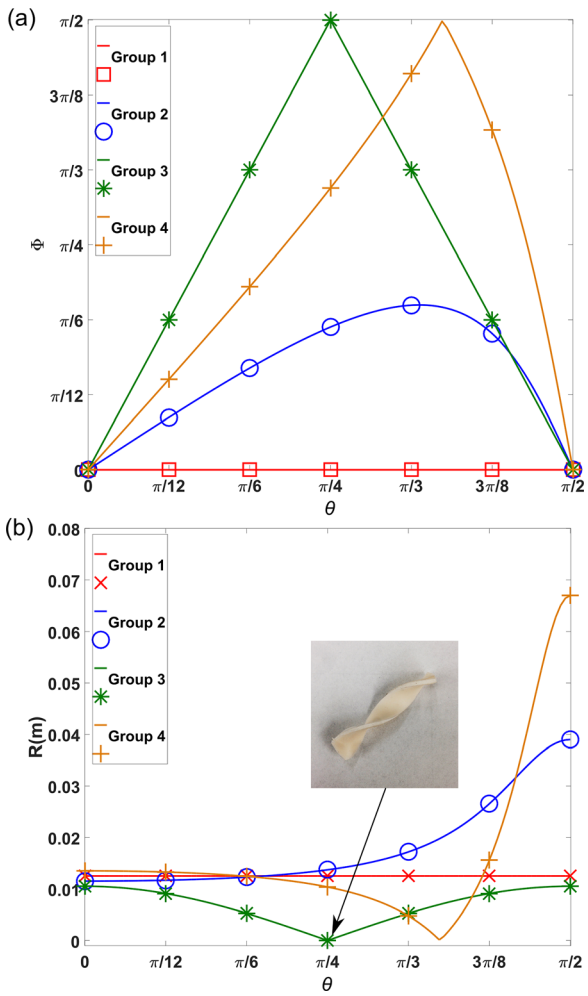

FIG. 4. (a) Helix angles (Φ) for the four tested conditions with different misorientation θ values. (b) Helical radius (R) for the four groups with different misorientation θ values. Experimental values for κ_x and κ_y for each group were measured as (1) $\kappa_x = \kappa_y = 80\,\mathrm{m}^{-1}$ (2) $\kappa_x = 87\,\mathrm{m}^{-1}$, $\kappa_y = 25.6\,\mathrm{m}^{-1}$ (3) $\kappa_x = -\kappa_y = 95.2\,\mathrm{m}^{-1}$, and (4) $\kappa_x = 74\,\mathrm{m}^{-1}$, $\kappa_y = -15\,\mathrm{m}^{-1}$.

decreases as θ increases to $\pi/3$ and then increases again as θ increases to $\pi/2$. It is noted that the absolute value of radius at $\theta = 0$ is less than that at $\theta = \pi/2$, because $E_y > E_x$ and $\kappa_x > \kappa_y$.

In summary, this study identifies the influence of anisotropic material properties on shape formation and transition in helical ribbons. The dependence of the radius and helix angle on the misorientation angle is shown to be dramatically different from that in isotropic ribbons. Under the same equal-biaxial pre-stretching condition, ring shapes formed in isotropic ribbons transitioned into helical ribbons when the material properties became anisotropic. Under the mechanically anisotropic pre-stretching condition, a purely twisted ribbon forms when $\theta = \pi/4$ and the material properties were isotropic; the corresponding structure featuring anisotropic material properties became a helical ribbon with a non-zero radius. The addition of material anisotropy has enriched tunable features in the design of programmable matter for a wide range of engineering applications.

See supplementary materials for schematics of the helical ribbons with Nitinol wires and corresponding theoretical analysis.

Z.C. acknowledges supports from the startup fund from the Thayer School of Engineering at Dartmouth and the Society in Science - Branco Weiss fellowship, administered by ETH Zürich.

[1]A. Pirrera, X. Lachenal, S. Daynes, P. M. Weaver, and I. V. Chenchiah, J. Mech. Phys. Solids **61**(11), 2087–2107 (2013).
[2]S. Armon, E. Efrati, R. Kupferman, and E. Sharon, Science **333**(6050), 1726–1730 (2011).
[3]Y. Abraham, C. Tamburu, E. Klein, J. W. C. Dunlop, P. Fratzl, U. Raviv, and R. Elbaum, J. R. Soc. Interface **9**(69), 640–647 (2012).
[4]P. Marmottant, A. Ponomarenko, and D. Bienaimé, Proc. R. Soc. B **280**, 20131465 (2013).
[5]N. Chouaieb, A. Goriely, and J. H. Maddocks, Proc. Natl. Acad. Sci. U.S.A. **103**(25), 9398–9403 (2006).
[6]Y. Sawa, F. Ye, K. Urayama, T. Takigawa, V. Gimenez-Pinto, R. L. B. Selinger, and J. V. Selinger, Proc. Natl. Acad. Sci. U.S.A. **108**(16), 6364–6368 (2011).
[7]Z. Chen, C. Majidi, D. J. Srolovitz, and M. Haataja, Appl. Phys. Lett. **98**(1), 011906 (2011).
[8]X.-Y. Ji, M.-Q. Zhao, F. Wei, and X.-Q. Feng, Appl. Phys. Lett. **100**(26), 263104 (2012).
[9]S. Kim, W. Kim, H. Chung, and M. Cho, RSC Adv. **5**(117), 96387–96391 (2015).
[10]N. Hu, X. Han, S. Huang, H. M. Grover, X. Yu, L. Zhang, I. Trase, J. X. J. Zhang, L. Zhang, L. Dong, and Z. Chen, "Edge effect of strained bilayer nanofilms for tunable multistability and actuation," Nanoscale (published online).
[11]L. Zhang, E. Deckhardt, A. Weber, C. Schönenberger, and D. Grützmacher, Nanotechnology **16**(6), 655 (2005).
[12]L. Zhang, E. Ruh, D. Grützmacher, L. Dong, D. J. Bell, B. J. Nelson, and C. Schönenberger, Nano Lett. **6**(7), 1311–1317 (2006).
[13]S. J. Gerbode, J. R. Puzey, A. G. McCormick, and L. Mahadevan, Science **337**(6098), 1087–1091 (2012).
[14]T. Savin, N. A. Kurpios, A. E. Shyer, P. Florescu, H. Liang, L. Mahadevan, and C. J. Tabin, Nature **476**(7358), 57–62 (2011).
[15]Z. Chen, Nanoscale **6**(16), 9443–9447 (2014).
[16]J. V. Selinger, M. S. Spector, and J. M. Schnur, J. Phys. Chem. B **105**(30), 7157–7169 (2001).
[17]R. Oda, I. Huc, M. Schmutz, S. J. Candau, and F. C. MacKintosh, Nature **399**(6736), 566–569 (1999).
[18]L. Teresi and V. Varano, Soft Matter **9**(11), 3081–3088 (2013).
[19]T. Gibaud, E. Barry, M. J. Zakhary, M. Henglin, A. Ward, Y. Yang, C. Berciu, R. Oldenbourg, M. F. Hagan, D. Nicastro, R. B. Meyer, and Z. Dogic, Nature **481**(7381), 348–351 (2012).
[20]J. S. Bunch, A. M. van der Zande, S. S. Verbridge, I. W. Frank, D. M. Tanenbaum, J. M. Parpia, H. G. Craighead, and P. L. McEuen, Science **315**(5811), 490–493 (2007).
[21]I. W. Hamley, A. Dehsorkhi, V. Castelletto, S. Furzeland, D. Atkins, J. Seitsonen, and J. Ruokolainen, Soft Matter **9**(39), 9290–9293 (2013).
[22]J. J. Abbott, K. E. Peyer, M. C. Lagomarsino, L. Zhang, L. Dong, I. K. Kaliakatsos, and B. J. Nelson, Int. J. Rob. Res. **28**(11–12), 1434–1447 (2009).
[23]Z. Tian, L. Zhang, Y. Fang, B. Xu, S. Tang, N. Hu, Z. An, Z. Chen, and Y. Mei, "Deterministic Self-Rolling of Ultrathin Nanocrystalline Diamond Nanomembranes for 3D Tubular/Helical Architecture," Adv. Mater. (published online).
[24]G. Hwang, C. Dockendorf, D. Bell, L. Dong, H. Hashimoto, D. Poulikakos, and B. Nelson, Int. J. Optomechatronics **2**(2), 88–103 (2008).
[25]Q. Guo, E. Dai, X. Han, S. Xie, E. Chao, and Z. Chen, J. R. Soc. Interface **12**, 20150598 (2015).
[26]J. Liu, J. Huang, T. Su, K. Bertoldi, and D. R. Clarke, PloS One **9**(4), e93183 (2014).
[27]J. Huang, J. Liu, B. Kroll, K. Bertoldi, and D. R. Clarke, Soft Matter **8**(23), 6291–6300 (2012).
[28]J.-S. Wang, X.-Q. Feng, G.-F. Wang, and S.-W. Yu, Appl. Phys. Lett. **92**(19), 191901 (2008).
[29]Z. Chen, Arch. Appl. Mech. **85**(3), 331–338 (2015).
[30]Q. Guo, H. Zheng, W. Chen, and Z. Chen, J. Mech. Med. Biol. **13**(06), 1340018 (2013).
[31]Q. Guo, A. K. Mehta, M. A. Grover, W. Chen, D. G. Lynn, and Z. Chen, Appl. Phys. Lett. **104**(21), 211901 (2014).

[32]Z. L. Wu, M. Moshe, J. Greener, H. Therien-Aubin, Z. Nie, E. Sharon, and E. Kumacheva, Nat. Commun. **4**, 1586 (2013).
[33]J.-S. Wang, G. Wang, X.-Q. Feng, T. Kitamura, Y.-L. Kang, S.-W. Yu, and Q.-H. Qin, Sci. Rep. **3**, 3102 (2013).
[34]Q. Ge, H. J. Qi, and M. L. Dunn, Appl. Phys. Lett. **103**(13), 131901 (2013).
[35]Z. Chen, G. Huang, I. Trase, X. Han, and Y. Mei, Phys. Rev. Appl. **5**(1), 017001 (2016).
[36]A. G. Shtukenberg, Y. O. Punin, E. Gunn, and B. Kahr, Chem. Rev. **112**(3), 1805–1838 (2012).
[37]B. Crist and J. M. Schultz, Prog. Polym. Sci. **56**, 1–63 (2016).
[38]Z. Chen, Q. Guo, C. Majidi, W. Chen, D. J. Srolovitz, and M. P. Haataja, Phys. Rev. Lett. **109**(11), 114302 (2012).
[39]W. Zeng, G. Liu, Y. Kitamura, and H. Nguyen-Xuan, Eng. Fract. Mech. **114**, 127–150 (2013).